Anal Bioanal Chem (2006) 386: 759–764
DOI 10.1007/s00216-006-0469-3

ORIGINAL PAPER

Noritada Kaji · Ryo Ogawa · Akio Oki · Yasuhiro Horiike · Manabu Tokeshi · Yoshinobu Baba

Study of water properties in nanospace

Received: 27 January 2006 / Revised: 3 April 2006 / Accepted: 5 April 2006 / Published online: 25 May 2006

Abstract Here we report an anomalous behavior of water, especially its viscosity and hydrodynamic flow, in a nanometer-confined space. As a typical model of a nanometer-confined space, the nanopillar chip, which was developed for DNA size-based separation was used, and single-particle tracking (SPT) technique was applied to investigate water viscosity and hydrodynamic flow in the nanopillar chip. The diffusion coefficients of nanospheres were almost one-third of the theoretical value derived from the Stokes-Einstein equation. This result gave indirect proof that water viscosity in a nanometer-confined space is higher than in a bulk solution. In order to improve resolution and throughput of the nanopillar chip for DNA separation, these potential factors affecting performance should be seriously considered.

Keywords Diffusion coefficient · Nanospace · Nanoparticles · Single-particle tracking · Nanopillar chip

Abbreviations SPT: Single-particle tracking · ICP: Inductively coupled plasma

N. Kaji (✉) · M. Tokeshi · Y. Baba
Department of Applied Chemistry,
Graduate School of Engineering,
Nagoya University,
Furo-cho, Chikusa-ku,
Nagoya 464-8603, Japan
e-mail: kaji@apchem.nagoya-u.ac.jp
Tel.: +81-52-7894611
Fax: +81-52-7894666

R. Ogawa · A. Oki · Y. Horiike
Nanomaterials Laboratories,
National Institute for Materials Science,
1-1, Namiki,
Tsukuba 305-0044, Japan

Y. Baba
Health Technology Research Center, National Institute of Advanced Industrial Science and Technology,
Hayashi-cho 2217-14,
Takamatsu 761-0395, Japan

Noritada Kaji
is Assistant Professor in the Department of Applied Chemistry at Nagoya University. His current research interests are mainly divided into three parts: nano-biodevices for DNA analysis, single molecule biophysics, and biological process on μTAS.

Introduction

Nanotechnologies, especially top-down approaches to construct nanometer-sized structures, have made it possible to fabricate sub-micrometer-sized channels and structures on silicon and quartz substrate. Now the sub-micrometer channels and structures are available for not only mechanical and electrical engineers but also analytical chemists. Nanospace, more precisely sub-micrometer space, is a quite interesting space especially for biophysicists because most biomolecules are nanometer-sized and are expected to show novel physical effects in nanospace [1–5]. What is more, a variety of studies of the physicochemical properties of liquids confined in nanospace have been performed, and it is indicated that liquid properties change in nanospace as compared with bulk. Tas et al. determined the negative pressure in nanochannels from the liquid meniscus [6] and Liu et al. gave an insight into unique properties in a confined liquid through the measurement of ion transport [7] and proton conductivity [8]. Tsukahara et al. proposed water structures in nanochannels based on NMR study [9, 10] and Hibara et al. investigated liquid viscosity and conductance in nanochannels by time-resolved fluorescence measurements [11]. Water confined in carbon nanotubes, which give an ultimately confined nanospace, has also been extensively studied experimentally [12, 13] and computationally [14]. These changes in liquid proper-

ties are of great interest in basic science. In order to develop our DNA separation method using the nanopillar chips, several investigations into hydrodynamic properties in nanospace are necessary to improve resolution and throughput. Since the surface area of the nanopillar chip is much larger than simple channel structures, it is readily understood that such a large, charged surface area raises complex electroosmotic flow and adsorption probabilities and may affect the analysis [15].

To investigate the liquid properties, we applied the single-particle tracking (SPT) technique to measure water viscosity in nanospace. A major advantage of the SPT technique is the ability to classify modes of Brownian motion of individual particles. Using this technique, it has been observed that individual membrane proteins or lipids in the plasma membrane of cells show a variety of types of motion, such as normal diffusion, directed diffusion, and restricted diffusion [16–18]. This variety of motions has been attributed to the presence of a random energetic trap array with different binding energies. In an ensemble of long-time averages, the mean-square displacement as a function of time revealed characteristics of the motion. Additionally, the slope of a mean-square displacement vs. time plot would give the diffusion coefficient that reflects the ambient viscosity. Taking these advantages into consideration, we applied the SPT technique to measure water viscosity and verify the presence of a hydrodynamic flow in nanospace.

Materials and methods

Device fabrication and design

The fabrication process of the nanopillar chip used here was the same described in our previous work [19] except the SiO_2 dry etching process. In this fabrication process, the quartz plate was etched by Cl_2 inductively coupled plasma (ICP). To investigate liquid properties in nanospace using SPT technique, the use of a quasi two-dimensional plane that allows observation of two-dimensional single-particle motion, would be preferable. From this standpoint, a shallow channel is preferable to let the molecules move in a quasi two-dimension plane. In addition, to acquire the precise trajectories without any special optical systems, a shallow channel provides optimum observation space since the focal depth of the high-power objective lens is only a few hundred nanometers, e.g., 150 nm for 100x/1.3 NA

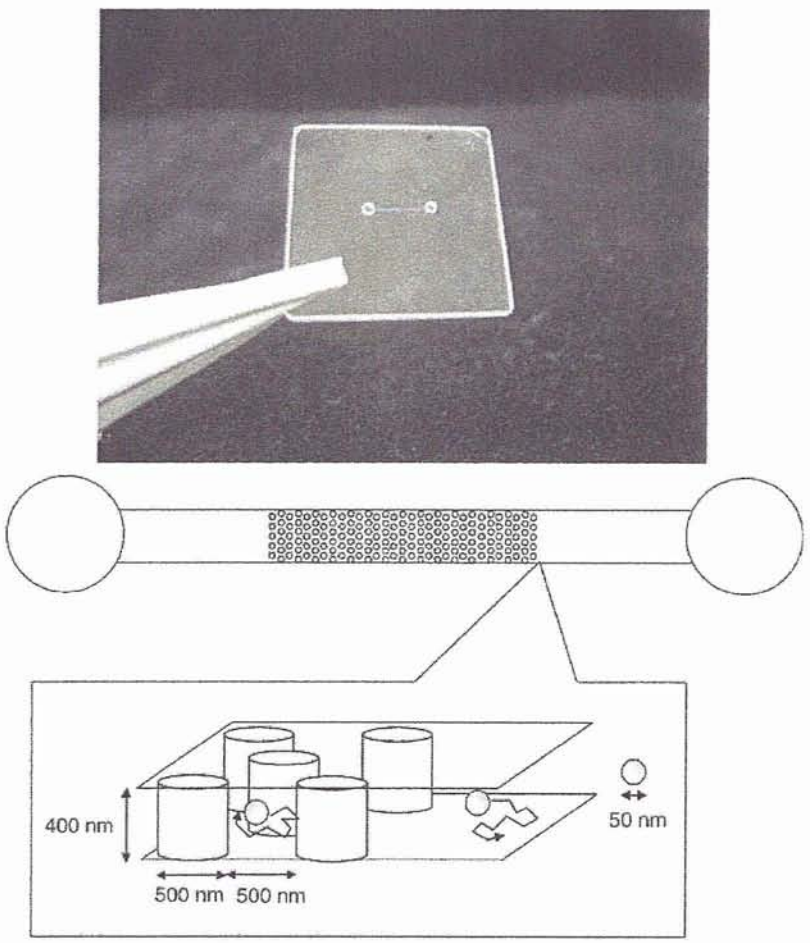

Fig. 1 Schematic representation of the nanopillar chip used for a single-particle tracking (SPT) measurement. The channel width and depth were 50 μm and 400 nm, respectively. Nanopillars were placed in the middle section of the channel, and their diameter, spacing and height were 500, 500, and 400 nm, respectively

objective lens. In order to observe the trajectories in this shallow channel through a 100x objective lens, a 0.17-mm-thick cover slip is required for the highest image resolution. Considering these points, a 400-nm-deep channel equipped with nanopillars in its middle section was fabricated on quartz substrates as shown in Fig. 1. The nanopillar diameter, spacing, and height used here were 500, 500, and 400 nm, respectively.

Single-particle tracking

Fluorescent polystyrene nanospheres with carboxylate groups on their surfaces (3.64×10^{14} particles/ml, 50 nm in diameter, Fluoresbrite YG Carboxylate Microspheres, Polysciences, Warrington, PA) were used as objective particles for measuring trajectory. The size and the ζ potential of nanospheres were confirmed by dynamic light scattering (DLS) and electrophoretic light scattering (ELS), respectively, using a dynamic light-scattering spectrophotometer (NICOMP 380/ZLS, Particle Sizing Systems, Santa Barbara, CA). Before the size measurement, the nanospheres were diluted 100-fold in deionized water and sonicated for 15 min to break up aggregates. The nanospheres had a diameter of 50.0±5.5 nm and a ζ potential of −44 mV in deionized water.

The chip was rinsed with 1 M HCl, 1 M NaOH and deionized water before use to remove any contaminants on the channel and the pillar surfaces. Owing to the treatment with sodium hydroxide, the minus-charged nanobeads could continue Brownian motion against adsorption on the surfaces. The washing procedure for nanopillar chips is one of the critical problems. In our first attempt, we tried to wash the nanopillar chip with a pressure-driven flow. But due to the infinitesimally small quantity of the solution in the nanopillar chip (~pl) and frangible nanopillars, this washing method seemed to be inappropriate. So we immersed the nanopillar chip in the solutions overnight, and after that, filled and evaporated the solutions in the nanopillar chip three to five times.

The nanospheres were diluted 10,000-fold in deionized water (~18 MΩ·cm) and sonicated for more than 10 min to break up aggregates and then applied to the reservoir. The water droplet containing nanospheres was put on one of the reservoirs and then was automatically introduced into the channel and the nanopillar region by capillary action. After the introduction of water was confirmed by an optical microscope, the single-particle tracking experiment was begun. The washing method mentioned above was applied to discharge the water from the channel and the nanopillar region. Single-particle trajectories were observed using a 100-W mercury arc lamp-illuminated inverted fluorescence microscope (Axiovert 135TV, Carl Zeiss, Tokyo, Japan) thorough a 100x/1.3 NA objective (Carl Zeiss). Brownian motion of nanospheres was captured by video-rate CCD camera (C7190-43, Hamamatsu Photonics, Hamamatsu, Japan), recorded on DV tape (DSR-11, SONY, Tokyo, Japan), and transferred to a computer. The centers of mass of fluorescent spots were analyzed and traced with image-processing software (Cosmos32, Library, Tokyo, Japan). All SPT measurement was done at 25 °C.

Table 1 Average diffusion coefficients (n=17) and their standard deviations at four different time intervals

Time intervals (ms)	Channel	Nanopillars
33	3.18±2.96	1.84±1.38
66	3.18±2.92	1.84±1.38
99	3.16±2.88	1.84±1.38
132	3.15±2.84	1.84±1.37

Results and discussion

Calibration of single-particle tracking

Quasi two-dimensional Brownian motion of nanospheres was traced from the sequential video images. The displacement of ith particle at time t, $\Delta x_i(t) = x_i(t) - x_i(0)$ and $\Delta y_i(t) = y_i(t) - y_i(0)$, gives the square displacement according to the following equation:

$$[\Delta R_i(t)]^2 = [\Delta x_i(t)]^2 + [\Delta y_i(t)]^2 \tag{1}$$

To obtain a diffusion coefficient, mean-square displacements $\langle R^2 \rangle$ should be calculated as a function of time:

$$\langle R^2 \rangle = \frac{1}{N}\sum_{i=1}^{N}[\Delta R_i(t)]^2 \tag{2}$$

where N is the total number of frames that have been traced (over 600 frames in this case). When the nanospheres undergo normal diffusion, the slope of the $\langle R^2 \rangle - \Delta t$ plot should be linear and $\langle R^2 \rangle$ can be expressed as follows:

$$\langle R_x^2 \rangle = 2D_x t \quad \langle R_y^2 \rangle = 2D_y t \tag{3}$$

$$\langle R^2 \rangle = \langle R_x^2 \rangle + \langle R_y^2 \rangle \tag{4}$$

$$2D_x t + 2D_y t = 4Dt \tag{5}$$

where D is the two-dimensional diffusion coefficient and D_x and D_y are one-dimensional diffusion coefficients for the x and y directions, respectively. Therefore, we could calculate the diffusion coefficient from the slope of the plot of $\langle R^2 \rangle - \Delta t$. While the diffusion coefficient can be obtained experimentally as mentioned above, the Stokes-Einstein equation also provides the diffusion coefficient of

a small particle based on thermodynamic and hydrodynamic views on diffusion. The equation is given by:

$$D = \frac{k_B T}{6\pi\eta r} \tag{6}$$

where k_B is Boltzmann's constant, T is the absolute temperature, η is the viscosity of the fluid and r is the radius of the diffusing particle. Comparing the diffusion coefficients obtained from Eqs. (5) and (6), we can estimate the differences in viscosity between bulk space and nanospace.

In membrane dynamic studies using SPT technique, as Kusumi et al. mentioned [18], the diffusion coefficient determined by SPT could provide the diffusion rate within membrane compartments that are only submicrometer-sized. Thus the authors refer to the diffusion coefficient estimated from SPT as the "microscopic" diffusion coefficient. In contrast, what we would like to investigate is the viscosity of water in nanospace based on the diffusion coefficient. It is the interactions between the nanospheres and the surrounding water that should be examined, not the nanospheres or the surfaces of the channel and the nanopillars. To prevent this, a lower concentration of nanospheres should be used for SPT measurement in the shortest possible time. In our microscopic observation system, the images were taken every 33 ms at 640×480-pixel resolution, with one pixel square being nearly equivalent to 120 nm^2. Considering the channel height (400 nm) and the spaces between nanopillars (500 nm), in order to validate SPT technique, a diffusion coefficient was first calculated by fitting the $\langle R^2 \rangle$ at time intervals of 33, 66, 99 and 132 ms over the whole observation time (20–30 s). The results are shown in Table 1. Differences between the means of the diffusion coefficients at each time interval were assessed with t-test. The diffusion coefficients did not change significantly in these time intervals. The averaged diffusion coefficients and their standard deviations show no significant differences among these time intervals. Though longer trajectory measurements are preferable to reduce the statistical errors yielded in the process of image analysis, trajectory measurements below 400 or 500 nm are preferred to exclude other factors that might influence a nanosphere's motion. Considering these points, diffusion coefficients at 132-ms time intervals were assumed to reflect the actual value.

Diffusion coefficients in nanospace

The diffusion coefficients at 132-ms time intervals were measured for 17 different particles over 20 s, and the diffusion coefficients of D_{channel}=3.15 μm^2/s in the nanochannels and $D_{\text{nanopillars}}$=1.84 μm^2/s in the nanopillars were obtained from the slope. These values could not be simply compared because geometrical differences, especially the area occupied by the 500-nm wide nanopillar itself and a difference in the interfacial area ratios, were not factors in the calculation. Although there was little difference between the interfacial area ratio in the nanochannel and the nanopillars (50×50 μm region, 5,040 μm^2/1,000 μm^3 in the nanochannel and 5,630 μm^2/1,000 μm^3 in the nanopillars), the degrees of freedom of possible trajectory in the nanopillars are obviously lower than in the nanochannels. Despite the differences in the degrees of freedom, we calculated the diffusion coefficients on the assumption that the nanopillars have zero volume but the same electrostatic properties as quartz.

Diffusion coefficients could be also estimated from Eq. (6), and the calculated value was D_{theory}=9.81 μm^2/s at 25 °C. Even if we could not simply compare the D_{channel} with the $D_{\text{nanopillars}}$, both of them are obviously smaller than the D_{theory}. The smaller diffusion coefficient suggested higher viscosity in the nanometer-high channels and the nanopillars. In keeping with the suggestions of Hibara et al. in their liquid introduction experiment [15], our SPT measurement also suggested that the viscosity of the liquid became higher in nanospace.

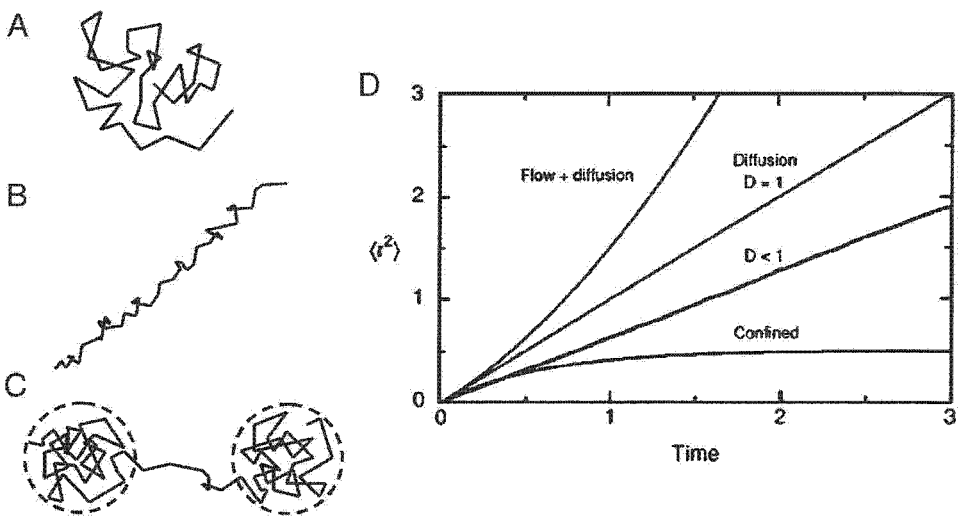

Fig. 2 Diagram of typical trajectories of different modes of motion: **a** simple diffusion, **b** directed motion, e.g., flowing beads under a hydrodynamic flow, and **c** confined motion, e.g., membrane proteins on the cell surface. **d** The relationship between the mean-square displacement $\langle r^2 \rangle$ and time t under various diffusion motions. This figure was reprinted, with permission, from the Annual Review of Biomolecular Structure, Volume 26 (c) 1997 by Annual Reviews http://www.annualreviews.org

Classification of modes of motion

While the SPT measurement over a short time period reflects a diffusion coefficient in microscopic surroundings, a long-time trajectory measurement over a few seconds gives several modes of motion of individual molecules: immobile, directed, confined, tethered, normal diffusion, and anomalous diffusion (Fig. 2) [16–18]. In the present study, the long-time observation of nanosphere motions and a classification of their motions would suggest the presence of a hydrodynamic flow under a geometrical confinement. Due to the simple geometry of the nanochannel and the nanopillars, the motions of nanospheres are expected to be classified into fewer modes than those observed in membrane dynamic studies. The main objective in this study was to investigate liquid properties in nanospace as well as the presence of a hydrodynamic flow in the nanochannel. In a microchip electrophoresis system without using polymer matrices, a difference in fluid level between the reservoirs generates a hydrodynamic flow and affects the resolution or the reproducibility of the separation. Nano-sized channels or nano-sized pillars, which had been suggested to increase the microscopic liquid viscosity, were expected to hold liquids tightly in their structures and prevent a hydrodynamic flow. In our previous study on DNA separation using nanopillar chips [19], it was practically impossible to detect a hydrodynamic flow in the nanopillar chips during DNA separation.

In this study, we classified the motion of nanospheres into the following three modes: simple diffusion, directed diffu-

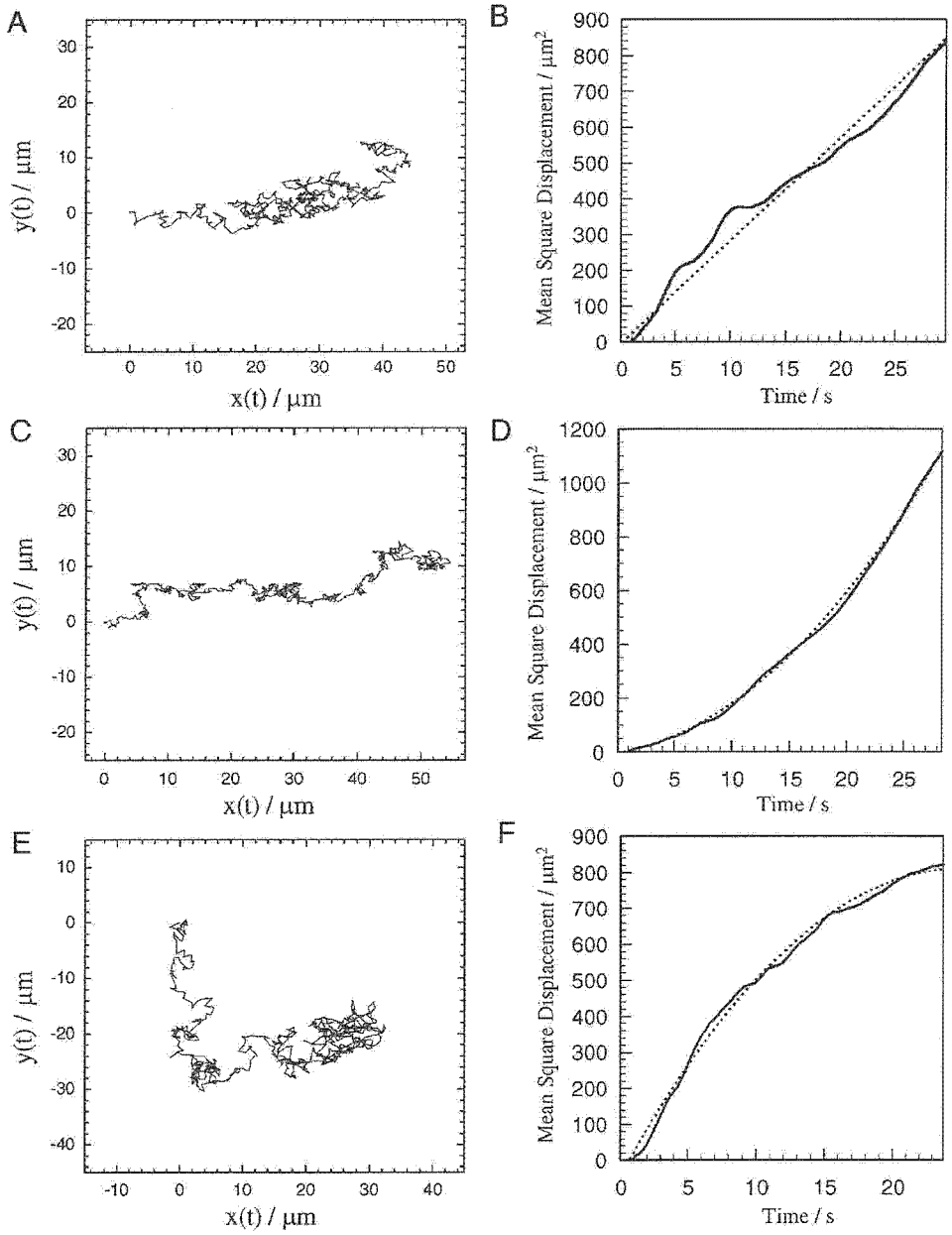

Fig. 3 Typical trajectories of nanospheres (**a**, **c**, **e**) and the corresponding plots (**b**, **d**, **f**). Based on the result of least-square fitting, plots were classified into three modes of motion: **b** simple diffusion, **d** directed diffusion, and **f** others

Table 2 The number of classified nanospheres with the percentage of total amount *in parentheses*

	Channel	Nanopillars
Simple diffusion	7 (41%)	9 (53%)
Directed diffusion	7 (41%)	4 (24%)
Others	3 (18%)	4 (24%)

sion, which implies the presence of hydrodynamic flow, and others. Fitting of $\langle R^2 \rangle - \Delta t$ was carried out by Levenberg-Marquardt method, and motions were classified based on the correlation factors. Figure 3 shows a typical trajectory of the nanospheres and their $\langle R^2 \rangle - \Delta t$ plot. These representative trajectories were drawn by connecting the positions of the nanospheres from the sequential video images. Though the trajectories were complex, the $\langle R^2 \rangle - \Delta t$ plot showed distinct differences among the modes. A total of 34 nanobeads, in the channel and the nanopillars, were analyzed to classify the motions. Consequently, as shown in Table 2, more directed diffusion was observed in the nanochannel than in the nanopillars. This result indicates that the nanopillars prevent a hydrodynamic flow to some extent even when the adjacent nanochannel has a hydrodynamic flow. Of course the nanopillars were not fully able to prevent the hydrodynamic flow, but relatively speaking, the degree of hydrodynamic flow was smaller than that in the channel. The low reproducibility of the DNA migration time in our previous work could possibly be attributed to the hydrodynamic flow or the different degrees of hydrodynamic flow in the channel and the nanopillars. The coexistence of a different degree of hydrodynamic flow in the nanopillar chips should be considered as one factor for achieving high-resolution DNA separation with an excellent reproducibility.

Acknowledgements The present work was partially supported by a Grant from New Energy and Industrial Technology Development Organization (NEDO) of the Ministry of Economy and a Grant-in-Aid for Scientific Research from the Ministry of Education, Science and Technology, Japan.

References

1. Turner SW, Cabodi M, Craighead HG (2002) Phys Rev Lett 88:128103
2. Han J, Turner SW, Craighead HG (1999) Phys Rev Lett 83:1688–1691
3. Han J, Craighead HG (2002) Anal Chem 74:394–401
4. Han J, Craighead HG (2000) Science 288:1026–1029
5. Cabodi M, Turner SW, Craighead HG (2002) Anal Chem 74:5169–5174
6. Tas NR, Mela P, Kramer T, Berenschot JW, van den Berg A (2003) Nano Lett 3:1537–1540
7. Pu Q, Yun J, Temkin H, Liu S (2004) Nano Lett 4:1099–1103
8. Liu S, Pu Q, Gao L, Korzeniewski C, Matzke C (2005) Nano Lett 5:1389–1393
9. Tsukahara T, Hibara A, Kitamori T (2005) Proc μTAS 2005:1255–1257
10. Tsukahara T, Hibara A, Kitamori T (2004) Proc μTAS 2004:189–191
11. Hibara A, Saito T, Kim HB, Tokeshi M, Ooi T, Nakao M, Kitamori T (2002) Anal Chem 74:6170–6176
12. Ohba T, Kanoh H, Kaneko K (2005) Nano Lett 5:227–230
13. Naguib N, Ye H, Gogotsi Y, Yazicioglu AG, Megaridis CM, Yoshimura M (2004) Nano Lett 4:2237–2243
14. Mashl RJ, Joseph S, Aluru NR, Jakobsson E (2003) Nano Lett 3:589–592
15. Xu XH, Yeung ES (1997) Science 275:1106–1109
16. Saxton MJ, Jacobson K (1997) Annu Rev Biophys Biomol Struct 26:373–399
17. Qian H, Sheetz MP, Elson EL (1991) Biophys J 60:910–921
18. Kusumi A, Sako Y, Yamamoto M (1993) Biophys J 65:2021–2040
19. Kaji N, Tezuka Y, Takamura Y, Ueda M, Nishimoto T, Nakanishi H, Horiike Y, Baba Y (2004) Anal Chem 76:15–22

ナノテクノロジーとバイオセンサ

各論 Ⅲ. マイクロチップ分析関連

3. 無痛針による微量採血分析から在宅で健康診断できるヘルスケアチップの開発

堀池 靖浩　甲田 裕子　小川 洋輝　長井 政雄

臨 床 検 査

第50巻 第12号 増刊号 別刷

2006年11月30日 発行

医学書院

各論 Ⅲ．マイクロチップ分析関連

3．無痛針による微量採血分析から在宅で健康診断できるヘルスケアチップの開発

堀池靖浩[1)]/甲田裕子/小川洋輝[2)]/長井政雄

〔KEYWORDS〕 無痛針，在宅診断，μTAS，ヘルスケアチップ，電気化学法，比色法

はじめに

わが国では近年，少子高齢化が進行し，高齢者が占める医療費のコストの激増が国家予算を圧迫するとともに，少子化による労働力の不足により国力を衰退させることが危惧される．この包括的解決の一策は，高齢者が働く意欲のある限り働き，培った知恵と経験を社会に還元できるよう元気で毎日を送れる「健康立国」を世界に先駆けわが国に創り出すことである．このためには予防が大切であり，簡便・迅速なバイオセンシング技術を早急に確立しなければならない．一方，μTAS (micro total analytical system)やLab on a Chip[1)]と呼ばれる小面積の基板に異なった分析部品を機能的に集積化して微量試料を分析する新研究分野が近年急激に発展し，その出口の1つとして種々のバイオチップの出現が期待されている．筆者らはその一貫として，微量の採血から在宅で簡便・確実に同時多項目を診断できる種々の診断用POCT(point-of-care testing)チップを開発している．図1にバイオチップ開発の目的とその展開をまとめたが，種々の診断チップが整うと，計測された多項目のマーカー値を医療施設に通信回線で送り，医療ブロードバンドネットワークと高精細ディスプレイを介して医師による問診が在宅で可能になる．検出マーカーを増やし，長期間の使用によって，医療施設に多数の方の健康・疾病マーカーの推移が蓄積されたデータベースが構築され，そのマーカーと疾病との相関関係を解明が可能になる．さらには，医師不在の寒村や離島の人々の遠隔診断が実現される．

本稿では，まず現在商用の各種POCT生化学分析装置を紹介し，筆者らの在宅検査を目指した無痛針から採取した微量の血液の電気化学法[2)]や比色法[3,4)]による分析によって健康・疾病マーカーを測定するヘルスケアチップを解説する．これらのバイオチップの製作については拙著[5)]に譲り，言及しない．

各種POCT生化学分析装置の現状

血液採取に基づくPOCT生化学分析装置として，現在，数社から血液の診断に基づいたバイオチップが実用化されている．ランセットと呼ばれる瞬間に指先を穿刺，採血し，血糖値の1項目だけ調べる血糖値モニターは，国内外とも多く販売され，糖尿病患者のPOCTに貢献している．一方，バイオチップとしては，米国のBiosite Triage Cardiac system[6)]は，マイクロ流路を基にしたデバイスを用いて全血から心臓病マーカーをPOC測定する．Micronics Inc.の「ORCAマイクロ流路プラットフォーム」は，拡散を基本にしたHフィルターやT-センサーなどのような種々の圧力駆動型マイクロ流体力学の要素部品を

1）HORIIKE Yasuhiro, KODA Hiroko　独立行政法人　物質・材料研究機構
2）OGAWA Hiroki, NAGAI Masao　アドビック(株)

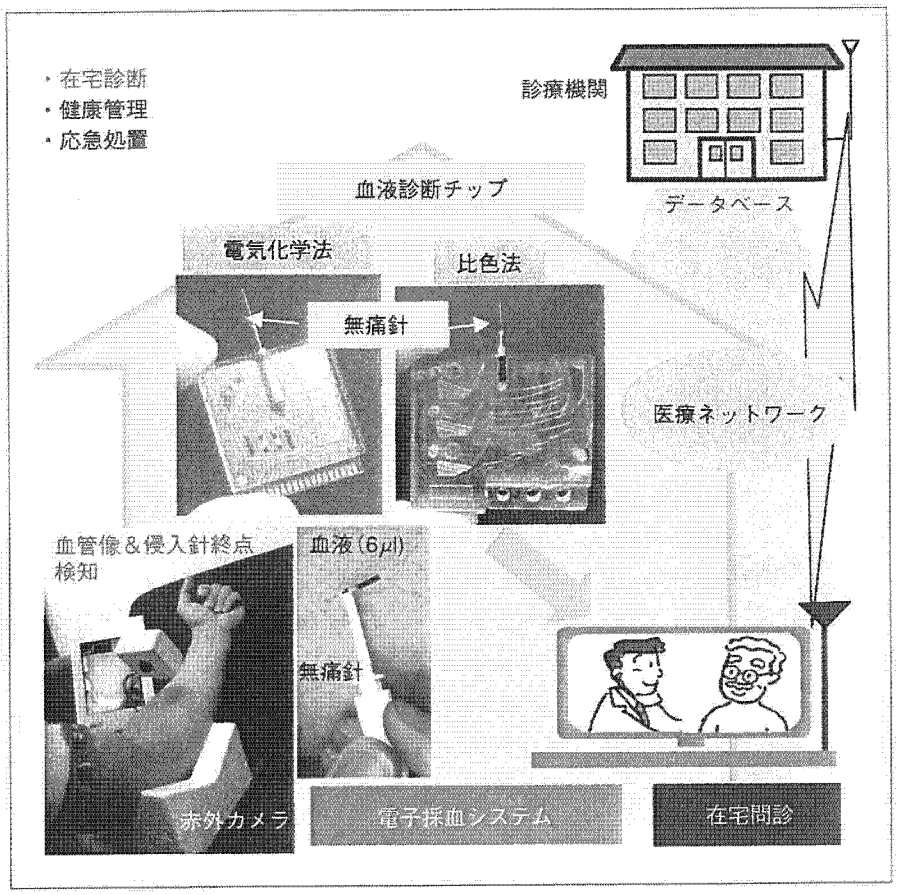

図1　バイオチップ開発の目的とその展開

図2　携帯型 i-STAT 分析器

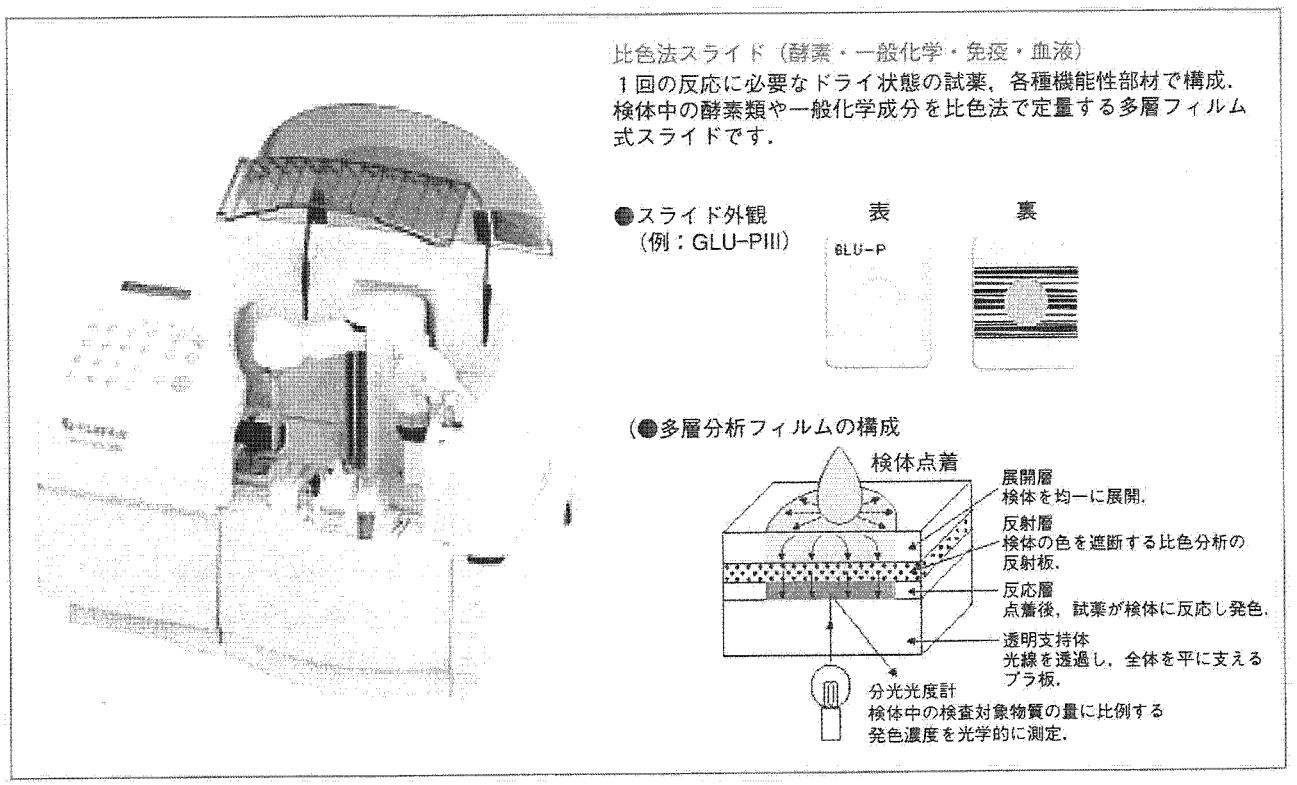

図3　富士写真フィルム社製ドライケミストリ分析装置

使い捨て可能なマイクロチップと結び付け，全血からイムノアッセイの POC 検査を行うチップを開発している[7]．

POC 検査のための最も普及しているマイクロ流体装置は，図2に示す携帯型 i-STAT 分析器である[8]．これは，約 100 μl の全血から電解質を

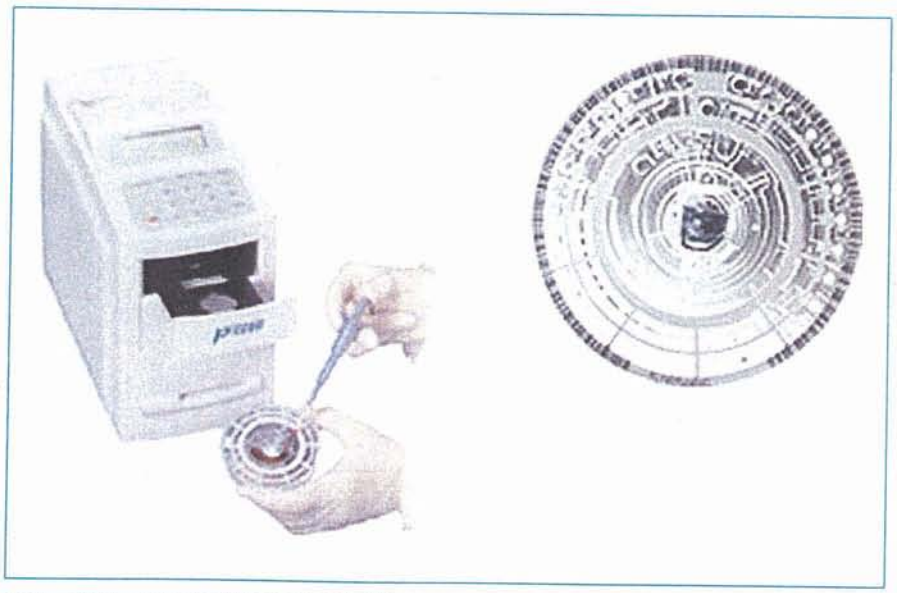

図4　米国 ABAXIS 社製血液分析装置

選択性電極法で，血液ガスを電極法で，グルコース，乳酸，尿素窒素やクレアチニンを酵素電極法で最大8項目が測定される．バイオセンサを集積化したカートリジに全血を導入し，測定器に挿入するとカートリジ内の較正液が圧力でキヤピラリバルブを開き，センサを較正し，空気を介して全血がセンサに導かれ，値が表示される．日本では同種のものがテクノメディカ社から販売されている[9]．同社からは，「ポケットリピッド」と称する電気化学式脂質検査も発売されている．これでは，10 μl の全血からコレステロール，中性脂肪，HDL，LDL の4項目が測定できる[9]．

上記の電気化学的検出法に対し，通常の自動血液検査装置に用いられている比色法を用いた小型装置も普及している．図3に示す富士写真フィルム社製ドライケミストリ法では，電解質，腎機能，脂質，肝機能，糖代謝，免疫など27項目が測定可能である[10]．ドライケミストリ法は，図3右に示すような構造の試薬スライド透明支持体上に分析反応に必要な試薬を含有した試薬層がコーティングされている．この試薬層には反応に必要な試薬が調製済みにし，ゲル中に乾燥した状態で保持されている．さらにこの上に反射測光を可能にする反射層と検体を均一に展開させる展開層が積層された4層構造になっている．このフイルムの上面に 10 μl 前後の血漿や血清の検体が展開層に滴下されると，検体は展開層の毛細管現象により横方向へ放射状に均一展開し，その後に反射層に浸透する．反射層およびゲルと混合された試薬層は血液成分を吸収し，単位面積当たりに一定量の検体を吸収して保持される．試薬層に吸収された検体と含有された試薬が反応し，検体成分に対応した発色を呈する．この呈色強度を支持体側から，発色に対応した特定の入射光を照射し，反射光の強度を測定することで，検体中の成分濃度を算出している．同種のものがアークレイ[11]から販売されている．

一方，図4の米国 ABAXIS 社製は，比色法の試薬を凍結乾燥し，それを右図に示すようなローターに設けた流路中に内蔵させ，左図に示すように血液を導入すると，遠心力で分離された血漿が毛細管現象で試薬に導入され，反応して呈色する[12]．すべての操作は遠心力で行われる．これで13項目溶液が測定できる．直接液体の試薬を用いた比色法では，最近，日立製作所パーソナル・ヘルスケアベンチャーカンパニーは図5に示すような装置を市場に出した[13]．血球分離用の遠心器は別扱いである．右図の一検体測定用のカートリジを導入して最大20項目が測定可能である．最近，比色法の試薬メーカの和光純薬社も同種のものを市販している．

図5　日立製作所パーソナル・ヘルスケアベンチャーカンパニー製血液分析装置

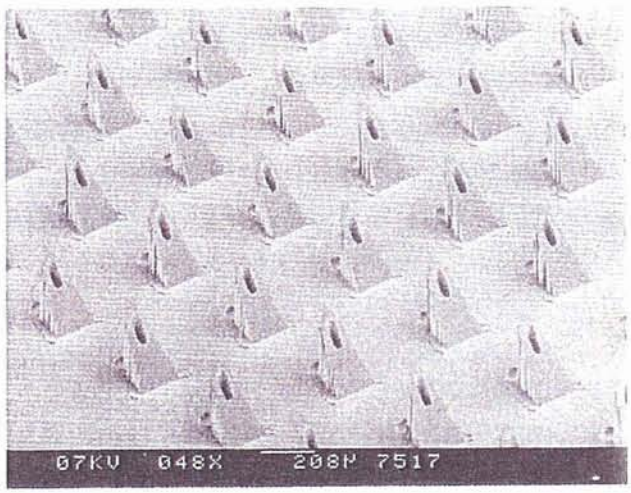

図6　MEMS で作製した中空微小針[14]

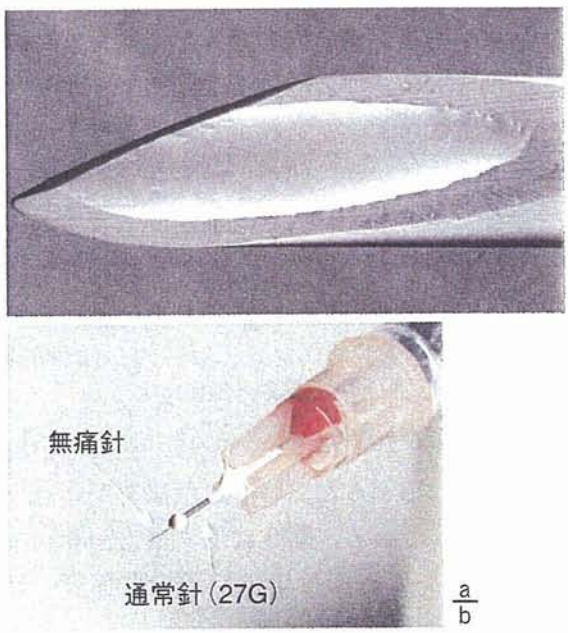

図7　150 μm 径の SUS 管製無痛針と通常の針との比較

採血器

上述したこれらの小型血液検査装置は，比較的多量の全血を要し，特に Pco_2 と Po_2 の測定には動脈から採血するので一般人は使用できず，医師に頼らねばならない．そこで，個人が在宅で簡単に微量の血液を採取して POCT 用に適用するためにはできるだけ低侵襲が不可欠である．この目的のために，MEMS 技術を駆使して多種の針が作られている[14]．この中で，図6に示す中空微小針はすでに商品化されている．開発者から直に聞いた話では，針のある表面を触ると「ざらざら」な紙の感触がし，指先から毛細管現象によりポンプなしで血液を無痛で取り出せるという．これは採血用よりむしろこれを貼布パッチに付けて薬剤を皮下に注入するために用いられている．このような構造は RIGA でも形成され，鋳型を形成後

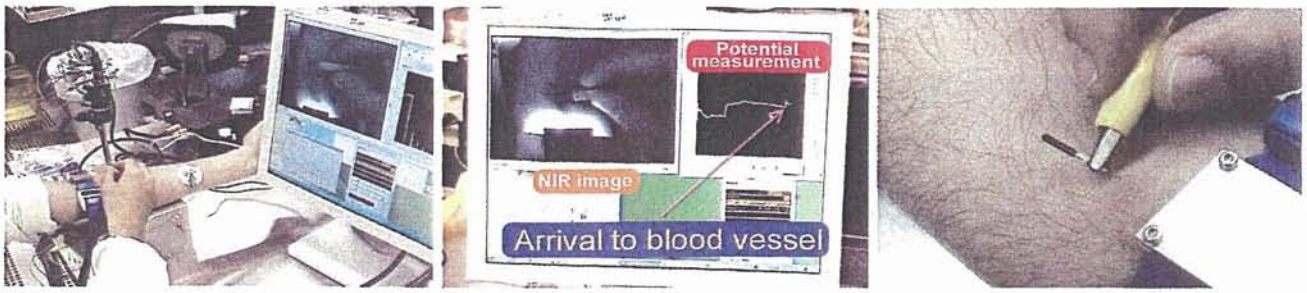

図8　電子採血補助装置による採血

a|b|c

高分子にモールドすることも研究されている．

しかし，上述の針はリンパ液などの体液も採取するため，正確な血液検査は難しく，やはり静脈などからの採血が望まれる．そこで，通常の皮膚への損傷と痛みを軽減するためには，まずは針径を小さくする必要がある．例えば，図7は，150 μm径のSUS管を用い，先端を10°に研磨し，端面を3面カットし，最後に電解研磨された針である．従来の針の外径の1/4程度なので，腕に刺しても痛みは感じない．さらに，粗い管の内壁を超平滑化した結果，針を皮膚に刺すと自分の血圧だけで採血できる．

しかし，静脈から採血する際，その所在が見えない場合が多い．そこで，近赤外光(near infrared；NIR, 850 nm)を照射して血管を可視化した．NIR光は水には透過し，皮下で拡散散乱して伝播するが，血液中のヘモグロビンには透過できず，血管の存在がわかる．さらに，皮膚表面から静脈の存在深さを知ることも重要である．その深さを知るため，針と皮膚表面との間に生じる電位を測定し，針が血管に到達したことを検出できるようにした[15]．この血管の位置と深さを知ることができたので，採血者は自分の腕と針アセンブリを見ず，ディスプレイ上でNIRイメージと電位変化を見て採血が可能になった．図8は，採血中の画面を示し，左側の画面でNIR光照射により静脈位置がわかり，右側の画面では針が皮膚に穿刺すると電圧は少し上がり，筋肉内の移動中は一定に保ち，静脈に達すると電圧は再び上がり，その時採血が始まったことを示している．将来的には画像処理を駆使して自動採血を目指す．

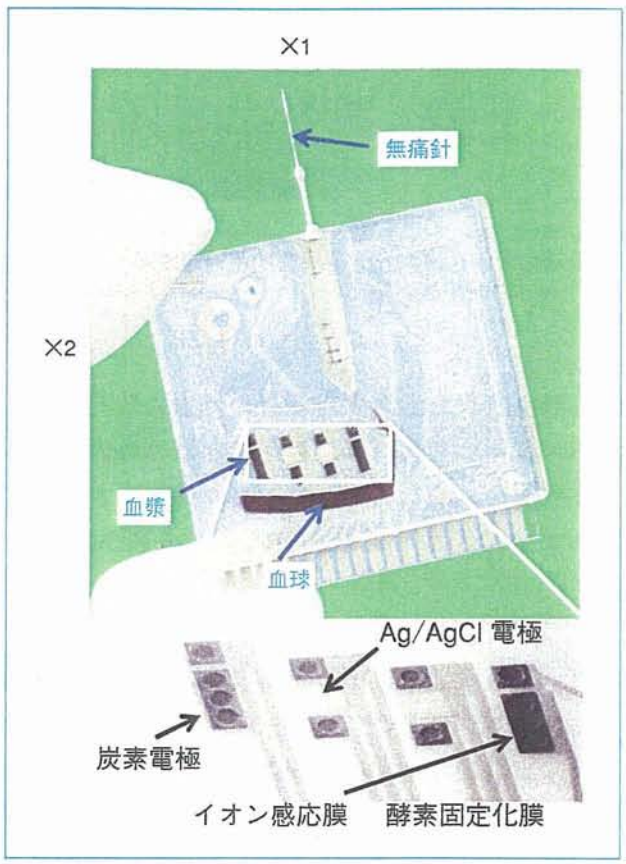

図9　電気化学測定用ヘルスケアチップと集積化バイオセンサ群の拡大写真

在宅で健康診断できるヘルスケアチップの開発

筆者らは，前述した無痛針により静脈より6 μlの微量血液を採取し，チップ上で遠心分離によって全血の血球成分と血漿成分の分離を行い，血漿成分を電気化学法，および比色法の2種類の方法により分析するヘルスケアチップを開発している．血球分離は，ガラスファィバーなどにより血球を捕獲する方法が使用されている場合もあるが，血漿の回収率が20%程度と低い．折角得た

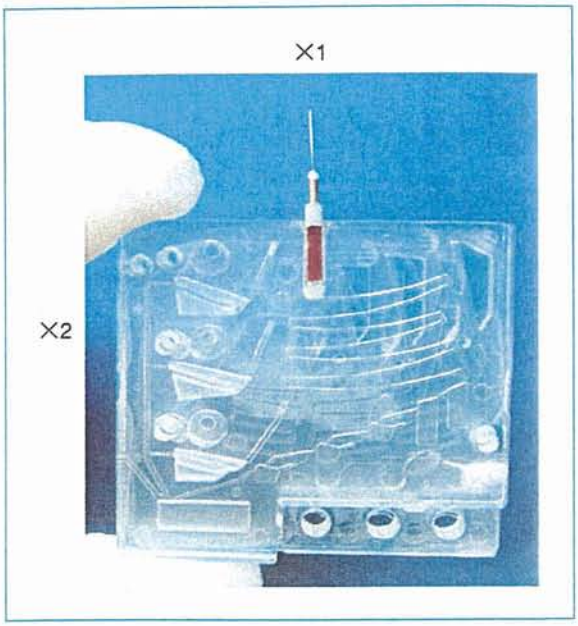

図10　6 μl 採血から3項目を比色測定するヘルスケアチップ

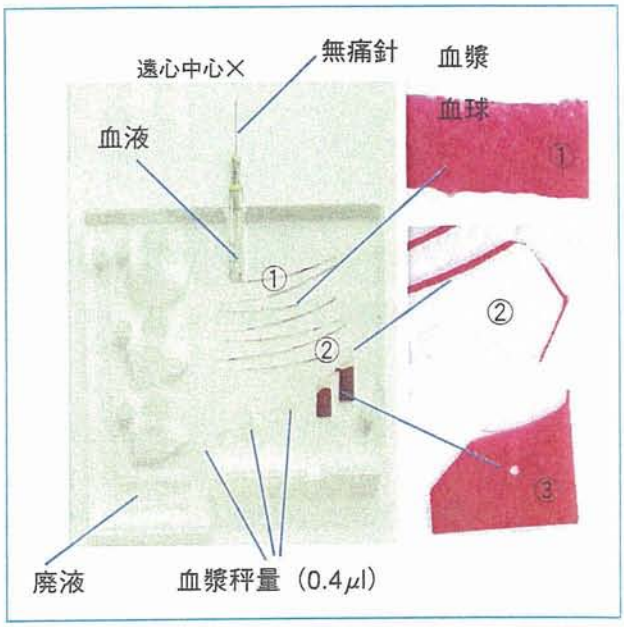

図11　ジグザグ流路による血球分離と血漿の同時秤量

血液から血漿を最大限得るためには古典的な遠心分離がよいと考え，また自己の血液は他人にとっては危険なものなので，いったん採血すれば手に触れずに操作させるため遠心搬送を採用している．

1．電気化学法チップ

電気化学法では，pH，Na^+，K^+ などの電解質イオン，およびグルコース，尿素窒素，クレアチニンなど健康マーカーの検出を目的としている．図9は電気化学測定用チップの写真を示す．集積化バイオセンサ群は拡大して示した．射出成型で形成したポリカーボネート製の流路用基板にポリエステル基板にスクリーン印刷法で形成した電極用基板を張り合わせた．センサ電極としてカーボン，非液絡型参照電極として銀/塩化銀，配線やパッドとして銀ペーストを用いて種々の電極を形成し，各部はマイクロ流路で結合されている．なお，チップ内流路表面は血球などの付着を抑制し，生態適合化を図るために生体膜表面を覆っているリン脂質膜を人工的に合成したMPCポリマー[16]を塗布してある．チップの動作は，図中の×1を中心に回転し，較正液をセンサ群への導入は，排出はチップを×2を中心に回転して行う．次に元の×1に図7の無痛針の採血後の血液溜めをチップに挿入し，元の×1を中心に回転するとチャンネルの下部に血球が，上部に血漿が分離され，血漿中のマーカーをバイオセンサで計測する．

バイオセンサとして，pHセンサは電解重合によりカーボン電極上に絶縁性ポリピロールを形成したもの，Na^+，K^+ イオンセンサとしてBis(12-crown-4)，Bis(benzo-15-crown-5)などのイオン感応膜とアニオン排除剤と可塑剤をTHF(tetrahydrofuran)で溶解したPVC(polyvinyl chloride)で固定化している．またグルコースは，まずVFc-co-HEMA(vinyl ferrocene 2-hydroxyethyl methacrylate)重合メディエータがカーボン電極への固定化され，その上にGA(グルタルアルデヒド)によってGOD(グルコースオキシダーゼ)を固定化した．血液尿素窒素(blood urea nitrogen；BUN)は，TD19C6イオノフォア/PVC/可塑剤(BBPA)/アニオン排除剤の構造によるアンモニアセンサを基盤にウレアーゼを固定化した．これらは自動のディスペンサーにより電極上に塗布される．ここでイオンセンサおよびBUNセンサは電位検知のポテンショメトリ法であり，グルコースセンサは電流検知のアンペロメトリ法で計測している[17]．これらの混合割合や固定化などには多くのノウハウが要求される．

2．比色法チップ

比色法チップでは，血清または血漿を基質緩衝液と混合し，例えばγ-GTPの場合は本来含有さ

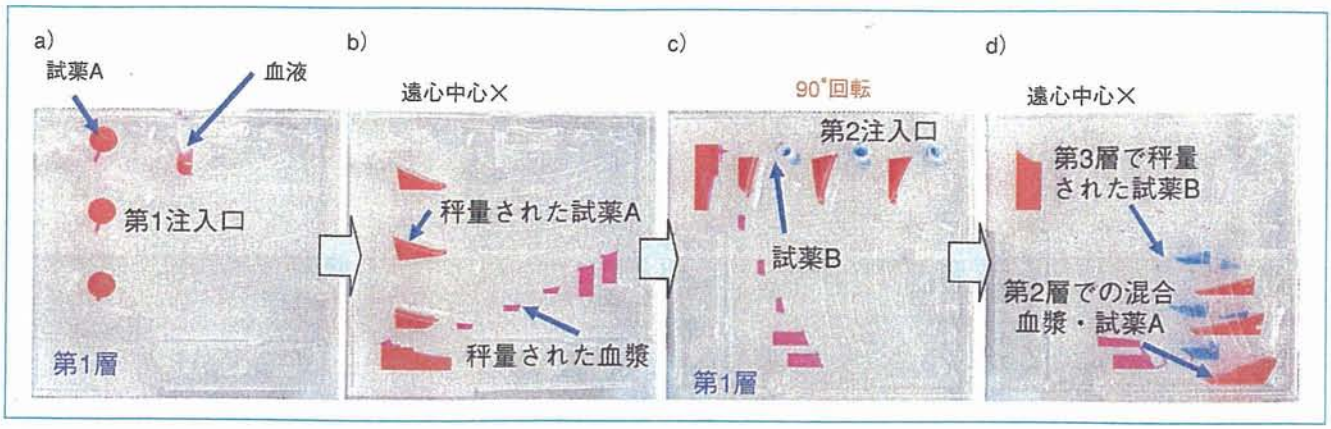

図12　試薬AとBの秤量と血漿とのミキシング過程

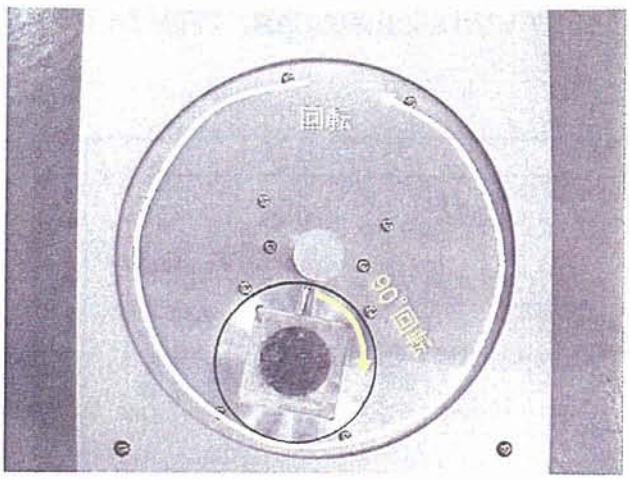

図13　チップに遠心力を与える公転・自転回転体

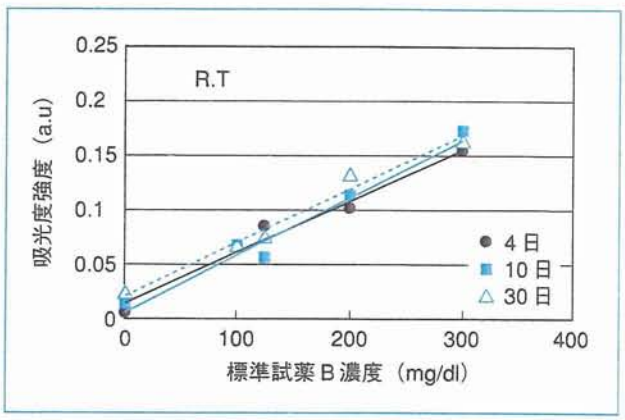

図14　中性脂肪凍結乾燥試薬B濃度と吸光度の経時変化

れている色素の光吸収(405 nm)を，GOTとGPTの場合は基質緩衝液に含まれているNADH(ニコチンアミドジニクレオチド)の光吸収(340 nm)を各酵素活性値に対して測定する．そのため，血漿と基質緩衝液を正確に秤量し，血漿：試薬＝1：50～100の高混合比を均一に混合することが必須である．しかし，一般にマイクロ流路内では，流体は層流となり混合は容易ではない．そこで，正確な秤量と均一混合を達成する比色法チップを開発した．本チップでは，電気化学法と同様，チップ動作は遠心力で行い，600 nmの波長のLED(light emitting diede)でコレステロール，中性脂肪，HDLの3項目を比色測定するため，6 μlの全血から分離した血漿を0.4 μl×3に同時秤量し，さらに1項目当たり2種類の試薬も秤量する．

図10は開発した比色法チップを示す．×1と×2は遠心力印加用の回転中心を示す．3層からなっている．無痛針に採取された血液を×1を中心に回転し，図11の1層目のジグザグ流路に導入し，血液を円弧から遠心力を受ける外側に配置されたジグザグの流路で，弱いが急速な加速で生じる遠心力によって，血漿は流路の上方に，血球は下方に分離され，最終段で，血球のみが捕獲され，血漿は0.4 μlに秤量されて採取される．次に，図12は試薬AとBの秤量と血漿とのミキシング過程を示す．血漿，および図12 aの左側の大きい孔から試薬Aを導入後，×1を中心に回転させ，1層目では血漿が，2層目では試薬Aが秤量される．図13は，チップに遠心力を与える回転体を示す．公転しチップが遠心力を受けた後，回転体上で90°自転させ，貯溜層で試薬Aと血漿を混合する．このようにして図12 bの状態から回転体上で90°自転させ，図12 cで試薬Bは1層目の小さい円筒状入口より導入され，2層目を通過して，×2を中心に回転させ，図12 dのように秤量される．試薬AとBでは，長期保存を目的に，2糖類のトレハロースを含有させ，

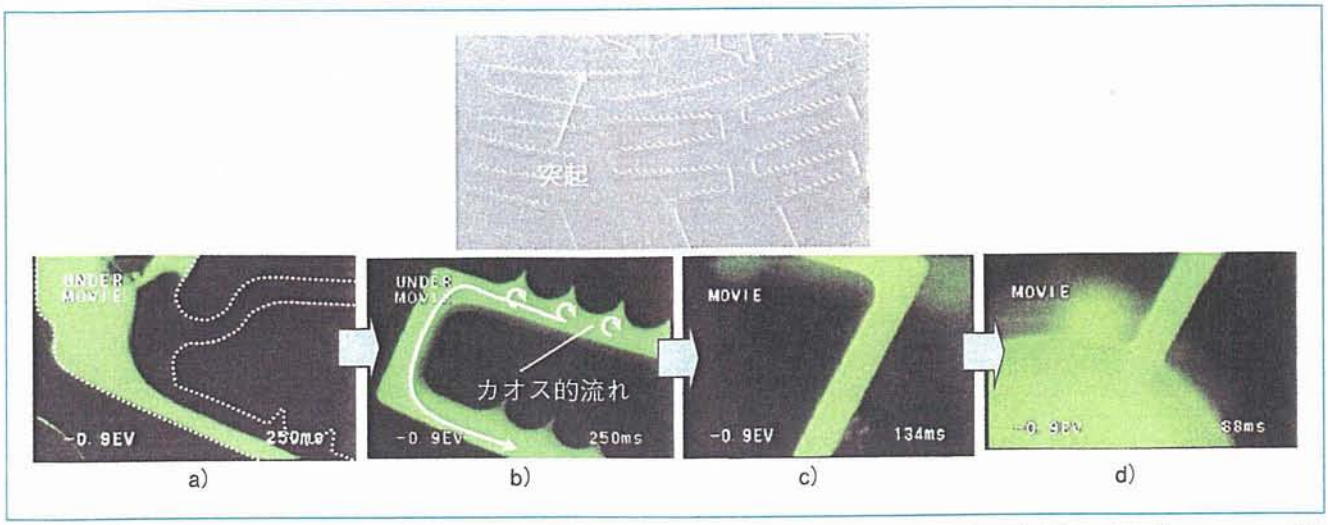

図 15　ジグザグ流路に試薬 A/血漿と試薬 B よるミキシング，(上図)3 チャンネルのジグザグ流路，(下図)ミキシング過程

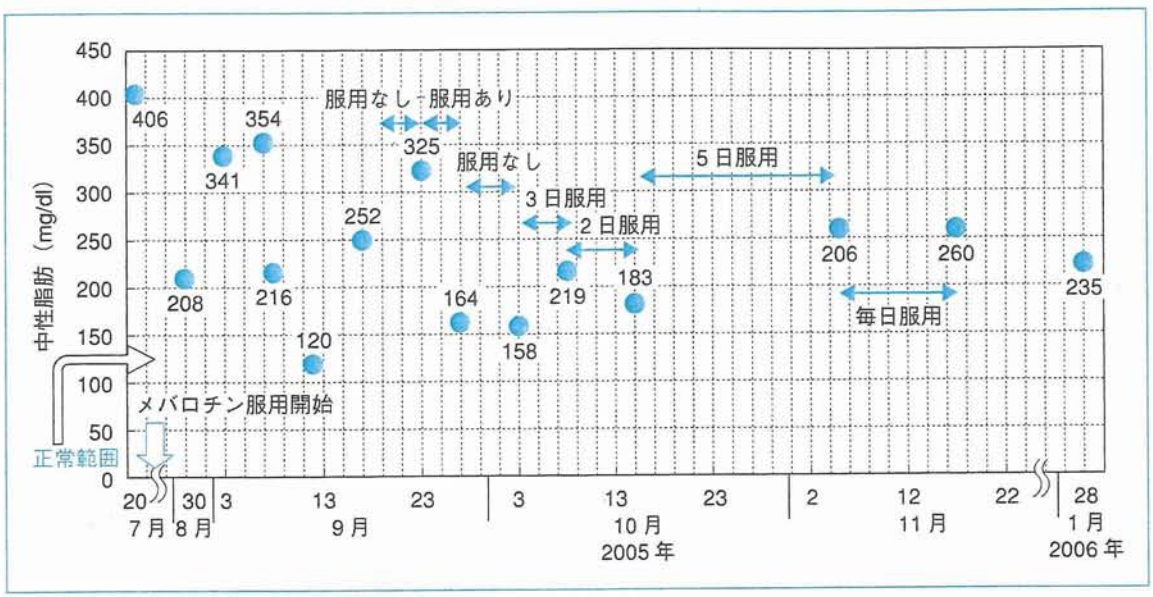

図 16　中性脂肪値のメバロチン服用効果

凍結乾燥したものを使用時に水で戻す試薬も開発した．図 14 は，中性脂肪測定用のトリグリセライド E-テストワコー(和光純薬)を本方法による試薬として用いたときの試薬量と吸光度の関係の経時変化を示す．1 か月を経ても劣化は見られない．

最終的には，図 15 a に示すように，試薬 A/血漿と試薬 B は 3 層目に設けられたジグザク流路内に×1 を中心に回転させ，図 15 b に示すように流路の内壁の一方に設けられた突起により乱流を発生させ，図 15 a では層流によりミキシングされていない溶液は，図 15 b から図 15 c を経て，図 15 d に示すように計測セル内に均一にミキシングされ比色計測が行われる．このジグザク流路の特徴は，流路の折返し部の前後で流路外側と内側の流れが入れ替わり，乱流を受けた液は，次段では乱流を受けず，逆に乱流を受けない液は次段では乱流を受け，次第にミキシングされていく．

上述した無痛針による電子的補助採血法，比色法診断チップ，今回開発したトレハロース包含試薬液を使用し，研究者の 1 人が異常に高い中性脂肪値を示し，その高脂血症治療薬であるメバロチンを内服しながら，今回開発したトレハロース包含基質緩衝液を用いて，4 か月に及ぶ服用効果をモニタリングした．図 16 にはこのように測定し

た中性脂肪値のメバロチン服用効果を示す．メバロチン服用前の中性脂肪値は406 mg/dlと高値であったが，メバロチン内服開始に伴い，中性脂肪値の漸減されていく様子が観察された．従来検査法による検証を行っていないため，診断チップによる測定値の精度・誤差に関して今後検討する必要があるものの，高脂血症治療薬による中性脂肪値の減少を捉えることに成功しており，本チップが簡易診断・モニタリング法として有用であることが示された．

今後の展望

診断チップを家庭に持ち込むためには，個人差にかかわらず無痛で確実に採血できるシステム，微量血液から正確に健康・疾病マーカーの測定，安価・小型・安全・簡単操作の測定器などが要求される．採血針では現在のSUS 304からSUS中のアレルギーを引き起こすNiを除いたSUS管の細管化も開発している．窒素アニールで剛性が向上し，より信頼性の高い無痛針が期待される．また，診断チップの検査項目は現状にさらに多項目を加え20項目程度には測定できるようにする．測定装置もCDプレイヤーのようなものにしたい．さらに，現在廃棄している血球成分から免疫検査，DNA解析などを行うため基礎研究もしている．種々のバイオチップによって診断機関と直結して在宅診断が実現すると，医療，さらには社会システムを大きく変革すると期待される．

文　献

1）Oosterbroek RE, van den Berg A (Eds)：Lab-on-a-Chip Miniturized System for (Bio) Chemical Analysis and Synthesis, Elsevier B. V. Netherland, 2003
2）Oki A, Takai M, Horiike Y, et al：Healthcare Chip Checking Health Condition from Analysis of Trace Blood Collected by Painless Needle. Jpn Appl Phys 42：3722-3727, 2003
3）Oki A, Ogawa H, Horiike Y, et al：Biochip Which Examines Function by Employing Colorimetric Method. Jpn Appl Phys 42：L 342-L 345, 2003
4）Horiike Y, Koda H, Chang S-H, et al：Colorimeric Measurement Clinical Chip for Home Medical Diagnosis, to be presented in μTAS 2006, Japan, 2006
5）堀池靖浩，宮原裕二：バイオチップとバイオセンサー，共立出版，2006
6）Biosite Inc：http:/www.biosite.com
7）Micronics Inc：http://www.micronics.com
8）i-STAT Corporation, http://www.abbottpointofcare.com/istat/
9）テクノメディカ：http://www.technomedica.co.jp/
10）富士写真フイルム：http://fms.fujifilm.co.jp/fms/drichem/
11）アークレイ：http://www.arkray.co.jp/index.html
12）ABAXIS：http://www.abaxis.com/
13）日立製作所パーソナル・ヘルスケアベンチャーカンパニー：http://www.hitachi.co.jp/products/personalhealthcare/index.html
14）Gardeniers JGE, Berenshot JW, de Boer MJ, et al：Digest IEEE Int. Conference on MEMS, Las Vegas, 53：20-24, 2002
15）Ogawa H, Nagai M, Horiike Y, et al：Blood Painless Collection System Equipping Detection functions for Search of Vein, *In* Northrup MA, Jensen KF, Harrison DJ (Eds)：Proc μTAS 2003, Tranducers Research Foundation, Squaw Valley USA, pp 741-744, 2003
16）Ishihara K, Oshida H, Ueda T, et al：Preparation of phospholipid polymers and their propertises as polymer hydrogel membrans. J Biomat Mat Res 26：1543, 1992
17）Oki H, Ogawa M, Horiike Y, et al：Development of healthcare chips checking life-style-related disease.Materials Science and Engineering C 24：837-843, 2004

Materials Science Forum Vols. 539-543 (2007) pp 4081-4086
online at http://www.scientific.net

Micro-Resistance Spot Welding of Nickel Free Austenitic Stainless Steel

Shinji Fukumoto[1, a], Taiju Matsuo[2], Daisuke Kuroda[3,b] and Harushige Tsubakino[1,c]

[1]Graduate School of Engineering, University of Hyogo, 2167 Shosha, Himeji, Hyogo 671-2201, Japan

[2]Graduate Student of University of Hyogo, 2167 Shosha, Himeji, Hyogo 671-2201, Japan

[3] Reconstitution Materials Group, Biomaterials Center, National Institute for Materials Science, 1-1 Namiki, Tsukuba, Ibaraki 305-0044, Japan

[a]sfukumot@eng.u-hyogo.ac.jp, [b] KURODA.Daisuke@nims.go.jp, [c]tubakino@eng.u-hyogo.ac.jp

Keywords: micro-resistance spot welding, nickel free stainless steel, delta-ferrite, weld lobe, joint strength, microstructure

Abstract

Micro-resistance spot weldability of nickel free stainless steel sheet was studied to fabricate medical implants. Weld lobe was established and the effect of welding parameters on joint strength was investigated. Weld nugget represented a rapidly quenched austenitic cellular structure whose cell size is several μm with a little ferrite. The amount of δ-ferrite in weld nugget is smaller than that predicted by some Schaefller diagrams due to rapid solidification during micro-resistance spot welding.

Introduction

Austenitic stainless steels such as SUS304 and SUS316L have been used for medical implants due to their superior corrosion resistance and mechanical properties. However, in general, these stainless steels contain nickel which is well known as a highly toxic element for human body, which encourages many researchers to develop specialized new material for medical implants [1-4]. Nickel free stainless steel has been developed for this reason and is one of promising materials [5-7]. Generally, since medical implants such as cardiac pacemaker, catheter and stent are very small and have complicate structure, it is difficult to fabricate them from single piece. Therefore, small-scale welding, so called micro-welding, processes are necessary to assemble them.

Resistance spot welding is well known as one of conventional 'large-scale' welding processes and often used in automobile industry. Therefore, we already have a lot of knowledge about resistance spot welding of steels. For the stainless steel, there are many researches on weldability in 'large scale' such as laser welding [8], arc welding [9] and so on. However, lots of problems such as electrode sticking, metal expulsion, non-repeatable welding and cooling rate that cannot be solved by simply scaling down from large to small scale lie ahead. Uenishi *et al.* reported the laser weldability of SUS304 stainless steel [10] and Ely *et al.* reported micro-resistance spot welding of cold rolled steel [11]. However, few researches on not only micro but also large scale welding of nickel free stainless steel have been reported.

The objective of this study is the elemental investigation such as establishment of weld lobe, joint reliability and microstructural development in micro-resistance spot welding of nickel free stainless steel.

Experimental procedure

Nickel free stainless steel of 200 μm in thickness was used in this study. It is made by the nitrogen absorption method that Fe-24Cr-2Mo stainless steel sheet was annealed at 1473 K for 3.6 ks in

nitrogen atmosphere. The details of nitrogen absorption method is described in ref.[5]. The chemical compositions of the steel with and without nitrogen are shown in Table 1.Tensile strength is 1167 MPa. Lap-welded joints were made using the steel coupons approximately 25 mm long and 7 mm wide. The coupons were joined by resistance spot welding as shown in Fig.1. The welding system consisted of MIYACHI Technos MH-D20A weld head (servo activated), and MIYACHI Technos MDB-2000 transistor type d.c. power supply. Flat-ended, round class II (Cu-Cr) electrodes, 3 mm in diameter were used. The welding force was set to 58.8 N. Welding current and weld time were varied from 400 to 2700 A and from 2.0 to 9.0 ms, respectively, with no current ramp-up or ramp-down times. Prior to welding, the sample surfaces were cleaned with acetone followed by polishing with emery paper.

Joint quality was evaluated by tensile shear testing. Diameter of nugget was determined from the fractured faying surfaces by stereoscope. Cross sections of the welds were also examined using optical microscopy. Metallographic samples for optical microscopy were prepared by electrolytic etching (4 V, 20 s) with a solution of 10% oxalic acid.

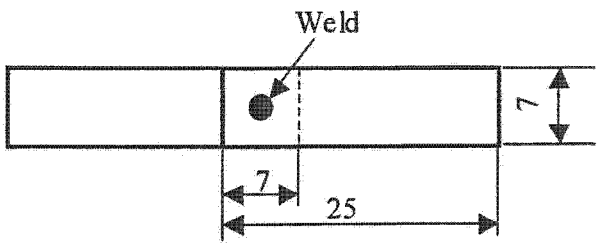

Fig.1 Schematic illustration of resistance spot welding set-up. (unit: mm)

Table 1 Chemical comopositions of nikel free stainless steels with and without nigrogen sbsorption, Fe-24Cr-2Mo and Fe-24Cr-2Mo-1N in mass%, respectively.

	C	P	S	Cr	Mo	O	N	Fe
Fe-24Cr-2Mo	0.002	0.002	0.0002	25.80	2.04	0.016	0.001	Bal.
Fe-24Cr-2Mo-1N	0.002	0.002	0.0002	25.80	2.04	0.016	0.92	Bal.

Results

Weld lobe

Fig.2 shows the cross sections of weld nugget with different welding currents. Nugget size increased with increasing welding current. At 800 A, nugget shape was irregular and the size was insufficient. On the contrary, nugget size and shape were favorable at 1400 A although weld metal expulsion occurred. In the present study, weld metal expulsion occurred on most welds, but it did not results in a reduction in joint strength as long as weld metal loss was not so much. By varying weld current, the results are presented on a graph (Fig.3) that plots welding current and the weld time. The parameters toward the center of lobe represent satisfactory welds selected for production welding. The lower curve represents the condition at which a specific minimum nugget diameter form while upper curve represents the conditions at which surface flash and electrode/sheet sticking occurred. If the minimum nugget is required, the minimum current needed is approximately 500 A for 9.0 ms of weld time. Fig.4 shows the relation between nugget diameter and shear force of the joint. All joints were fractured through nugget. The open circle plots represent the good welds shown in Fig.3 while crossed-marks represent the weld with severe surface flash and electrode sticking. The group of open circle shows good linear relation between shear force and nugget diameter. The tensile shear stress of nugget was estimated to about 650 MPa by the gradient, which would almost correspond to the maximum shear stress that was estimated by the tensile strength of base metal. On the other hand, when big surface flash occurred, nugget strength decreased in comparison with good welds. Most big surface flash occurred with electrode sticking and sever weld expulsion, resulting in reducing joint quality because of the loss of metal volume [12, 13]. Fig.5 shows the plots of shear force versus

welding current or weld time. Shear force increased as nugget grew with increasing welding current. Electrode sticking and surface flash started at a welding current of 1200 A. Shear forces drastically changed around 2.0 ms of weld time and then saturated with the condition of over 7.0 ms of weld time. Because contact resistance at faying surface that is main factor for heat generation decreased drastically at initial stage of weld process [14].

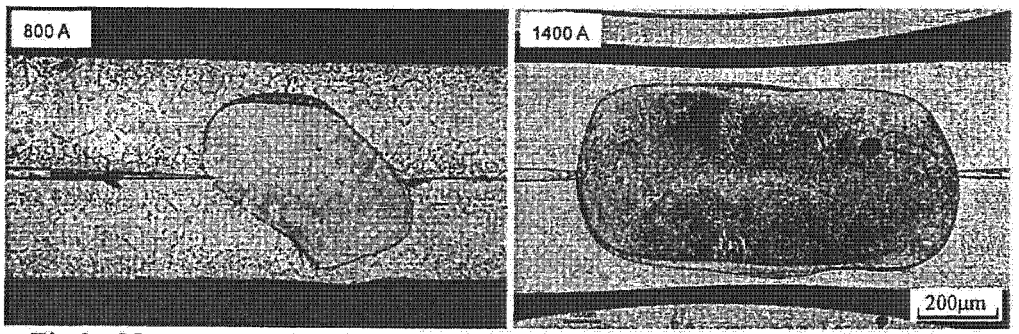

Fig.2 Nugget growth with increasing welding current for 9 ms of weld time.

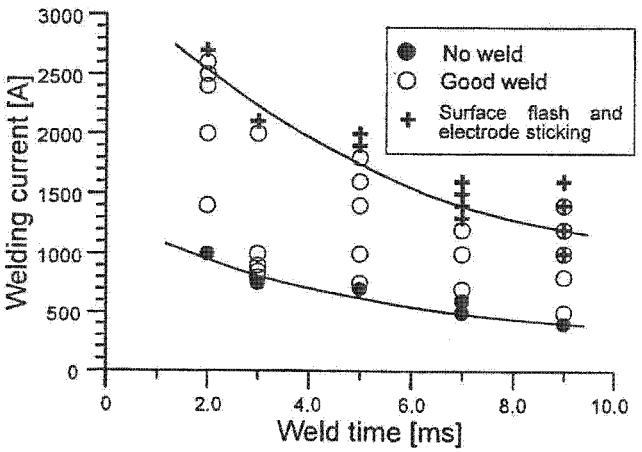

Fig.3 Weld lobe for micro-resistance spot welding of nickel free stainless steel sheet with 58.8 N of welding force.

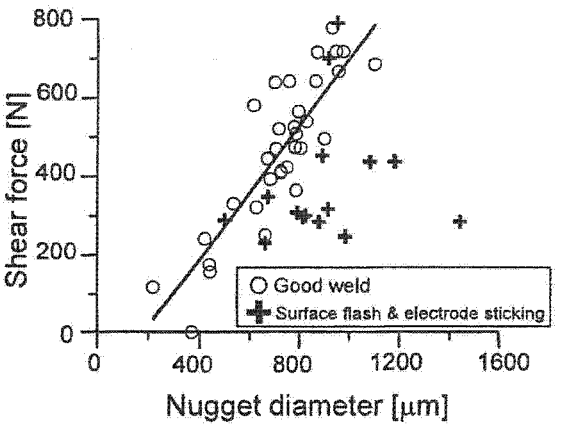

Fig.4 Shear force of joints versus nugget diameter.

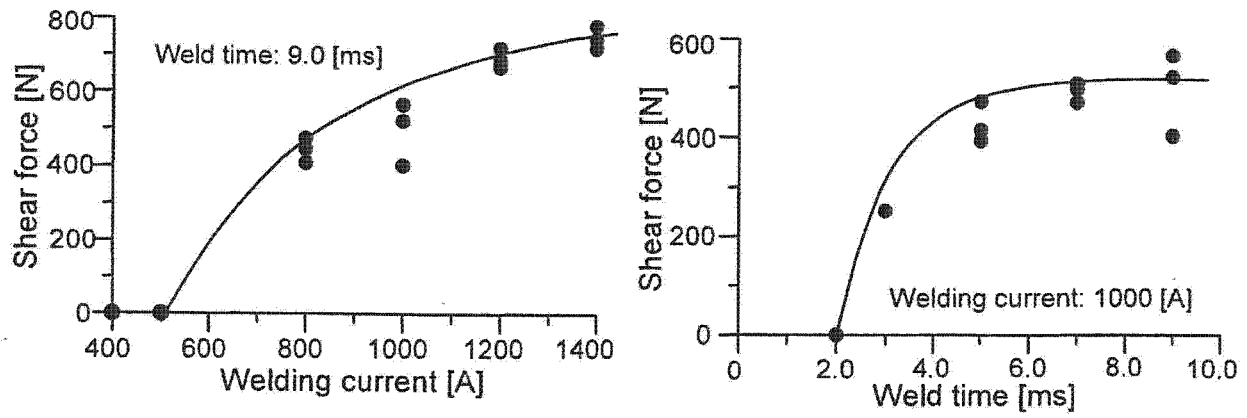

Fig.5 Effect of welding current and weld time on joint strength.

Microstructures

Fig.6 shows the microstructures of weld nugget and heat affected zone. The microstructure of weld nugget consisted of austenitic cellular dendrite or cellular structure that includes a little δ-ferrite. δ-ferrite, which is contrasted as dark, was slightly observed on the boundary of austenite cells (Fig.6d). The amount of δ-ferrite was approximately 5 to 7% on micrographs. The cell size changed by position, and it was approximately 1.0 to 2.6 μm which almost equal to that of laser welded stainless steel [10]. Any metallic carbides that often cause grain boundary corrosion were not observed in the heat affected zone by optical microscopy. As is well known the Schaefller diagram is convenient for predicting microstructure of weld metal.

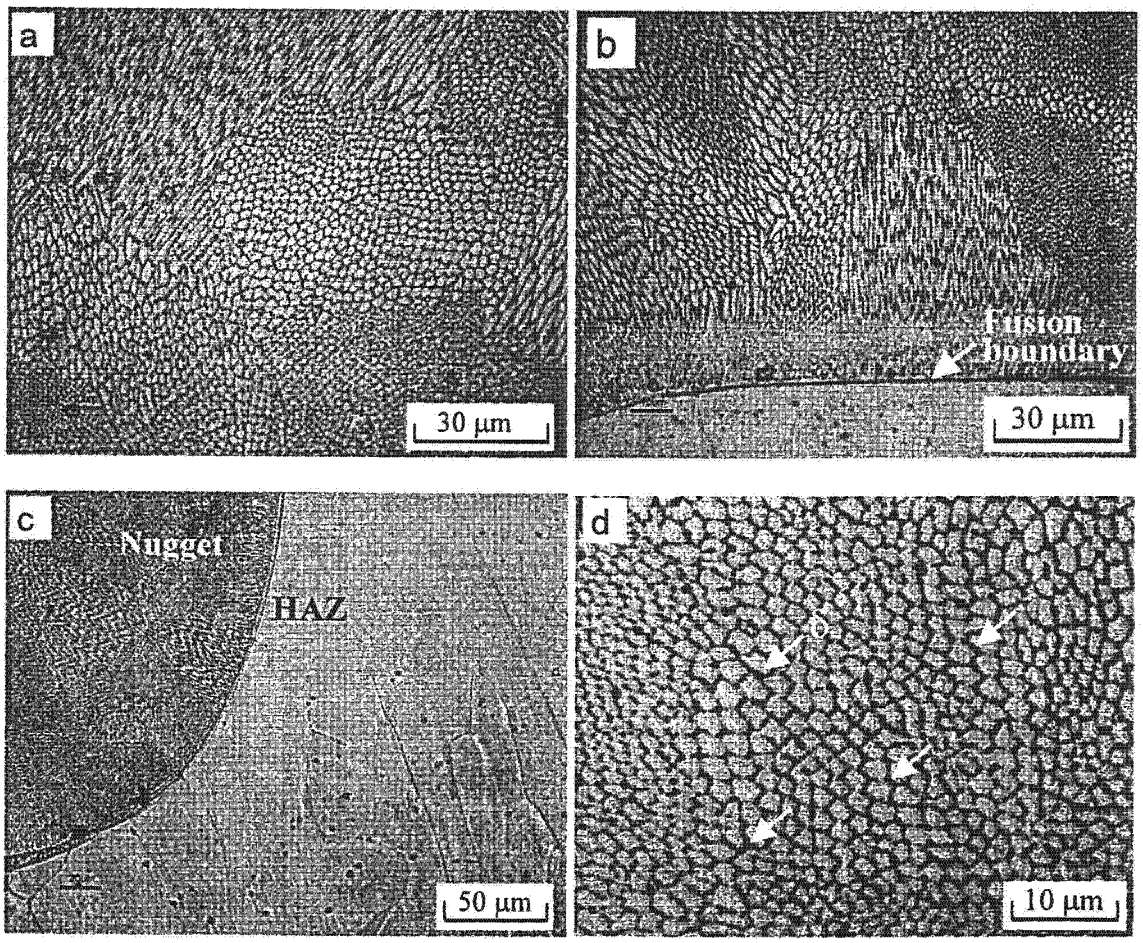

Fig.6 Microstructures of nugget and heat affected zone; (a) center of nugget, (b) near the fusion boundary, (c) heat affected zone and (d) higher magnification of cellular structure in weld nugget; δ-ferrite was observed on the boundary of austenite cell.

The composition of the nickel free stainless steel was plotted in Hull's and Hammar's diagrams whose nickel equivalent includes the effect of nitrogen (Fig.7) [15, 16]. Much more than 5% ferrite is predicted for the present material by either diagram, which is more than that was estimated on the optical micrographs. Although Hull's diagram looks more suitable to the present study than Hammar's, the experimental results did not correspond well to the predicted microstructures in either case. So a new modified diagram for the present nickel free stainless steel will be needed to predict weld nugget microstructures more accurately in the near future. Moreover, the cooling rate should be also considered to understand such less ferrite formation in the resistance spot welding. As shown in Fig.6,